Dielectric metasurfaces for refractive index sensing towards anemia detection

Dhananjoy De[1] and R. Vijaya[1,2]*

[1]Centre for Lasers and Photonics, Indian Institute of Technology Kanpur, Kanpur, Uttar Pradesh, India,
[2]Department of Physics, Indian Institute of Technology Kanpur, Kanpur, Uttar Pradesh, India

In this article, an all-dielectric metasurface-based refractive index sensor is proposed in the near-infrared wavelength regime. The sensor employs well known magnetic dipole and electric dipole resonances for sensing. We have also computationally demonstrated that sensitivity and figure of merit of the sensor can be enhanced by increasing the interaction between the electromagnetic field and the surrounding medium using a suitable design modification. The proposed improved sensor can be used in anemia detection and also to measure its progress as proposed in this work.

KEYWORDS

metasurface, all-dielectric, refractive index sensing, anemia detection, near-infrared detection

1 Introduction

The two-dimensional arrangement of scatterers constitutes a metasurface, especially when their size and periodicity are lesser than the wavelength. Ultrathin arrays of sub-wavelength scatterers in a metasurface can be used to control the amplitude, phase, and polarization of the electromagnetic (EM) waves. Using these metasurfaces, several applications have been proposed in topics such as wavefront engineering (Yu et al., 2011; Ni et al., 2012), meta-lenses (Aieta et al., 2012; West et al., 2014), imaging (Khorasaninejad and Capasso, 2017), polarization control (Shao et al., 2014; Gao et al., 2015), and sensing (Tittl et al., 2018; Zhang et al., 2022). Apart from metasurfaces with fixed properties, there are reports on active metasurfaces as well, which allow the user to tune the properties even after the device is fabricated (Horie et al., 2018; Howes et al., 2020).

Refractive index (RI) sensors based on metasurface designs are useful in environmental, chemical, biomedical, and biological sectors (Lee et al., 2017). In each case, different values of RI and different extent of change of RI are to be detected with high accuracy. Metallic nano-structure based RI sensor technologies have been very popular because of device miniaturization (Ozbay, 2006) and high sensitivity (Tong et al., 2014). However, metals have inevitable Ohmic losses, thus making all-dielectric counterparts always a better option (Baranov et al., 2017). Even though all-dielectric metasurface based high-sensitivity RI sensors have already been reported, there is a significant scope to improve the sensitivity, figure of merit (FOM) or the design itself for improving their commercial utility (Hu et al., 2017).

In this work, we present a design for all-dielectric metasurface-based RI sensor. We explore the performance of the sensor using numerical computations. The sensor shows dual spectral response in the wavelength range of 1.2 μm–1.7 μm. Such a dual response is an important advantage in any sensor as it provides dual options of tracking the changes. In addition, the dual-resonance feature also provides better sensing stability (Chen et al., 2023).
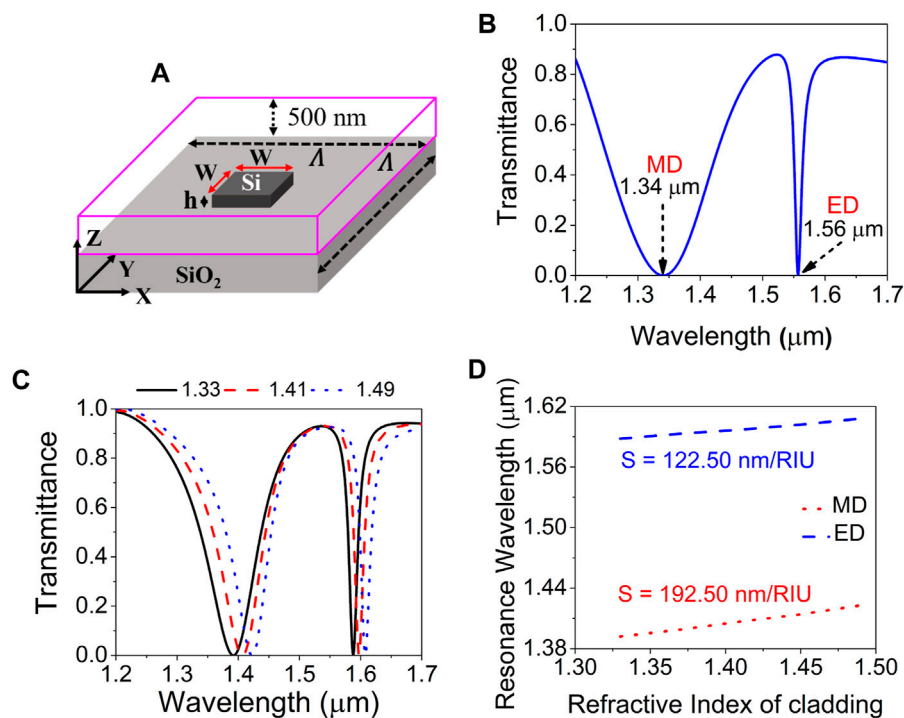
FIGURE 1
(A) Unit cell schematic of the all-dielectric metasurface sensor. **(B)** Computed transmission spectrum for a normally incident Y-polarized plane-wave excitation of the metasurface sensor with air as cladding material. **(C)** Computed transmission spectra of the all-dielectric sensor for three different RI of the surrounding medium. **(D)** Resonance wavelength shift for different values of cladding refractive index in the all-dielectric sensor.

In spite of the simple geometry, it offers reasonably good sensitivity and FOM. We then demonstrate how it can be improved with a small design change involving the shape of the scatterer. Effects of angle of incidence and state of polarization of the incident light on the sensor are also investigated. The geometrical parameters of the sensor are optimized to obtain the best sensitivity as well as FOM together. Further we demonstrate its application in anemia detection and evaluating the extent of its progress as well. In this work, all the numerical electromagnetic computations are performed using Rigorous Coupled Wave Analysis (RCWA) method (DiffractMod, 2004).

2 All-dielectric metasurface as refractive index sensor

The proposed all-dielectric metasurface sensor consists of an array of silicon (Si) scatterers. These square shaped scatterers of width (W) 570 nm and height (h) 220 nm are present on a semi-infinite silicon-dioxide (SiO_2) platform. The unit cell schematic of the all-dielectric sensor is shown in Figure 1A. A square-lattice arrangement with a periodicity (Λ) of 700 nm in XY-plane is considered here. The numerical computations are done for the unit cell with in-plane periodic boundary conditions. The non-dispersive refractive indices of Si and SiO_2 are taken as 3.70 and 1.48, respectively. Computed transmission spectrum of the metasurface for Y-polarized normally incident plane wave shows two minima at λ ~1.34 μm and λ ~1.56 μm (Figure 1B). The line-width of the

resonance at λ ~1.34 μm is very broad as compared to the line-width of the resonance at λ ~1.56 μm. To evaluate the origin of these resonances, we have computed the electric and magnetic field distributions in the YZ- and XZ-planes, respectively, with the cross-section of the Si pillar at its center. The spatial field distributions of $|E_y|$ and $|H_x|$ imply that the resonance at λ ~1.34 μm is of magnetic dipole (MD) type and the resonance at λ ~1.56 μm is of electric dipole (ED) type (Iwanaga, 2018).

To explore the metasurface as RI sensor, initially we have considered a cladding layer 250 nm thick with RI =1.33 for water on SiO_2 substrate. However, to study its effect fully, the thickness is increased up to 550 nm with a step of 100 nm and computed transmission spectra are shown (Supplementary Figure S1). As the cladding layer thickness increases, both the resonances shift to longer wavelengths. This shift is more in the case of MD resonance than in ED resonance. In addition, this shift is not a linear function of cladding thickness and nearly saturates after 450 nm of cladding thickness. So, we have considered an optimized cladding thickness of 500 nm. It is observed in Figure 1C that when the cladding thickness is 500 nm and cladding index is 1.33, MD and ED resonances appear at λ ~1.39 μm and λ ~1.59 μm, respectively. The refractive index of the cladding layer is changed from 1.33 to 1.49 and the transmission spectra are computed for Y-polarized normally incident plane wave. The transmission spectra of the sensor are shown in Figure 1C for three values of cladding RI.

The values of full-width at half-maxima (FWHM) for MD and ED resonances are ~95.8 nm and ~16.5 nm respectively, for a
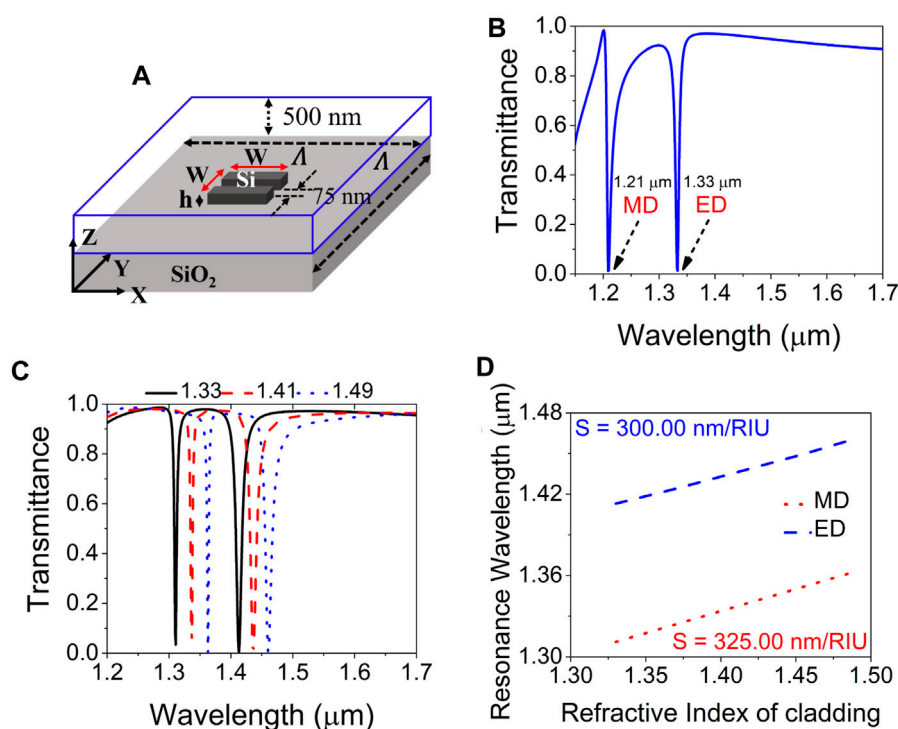
FIGURE 2
(A) Unit cell schematic of the improved sensor. **(B)** Computed transmission spectrum for a normally incident Y-polarized plane-wave excitation of the improved sensor with air as cladding material. **(C)** Computed transmission spectra of the improved sensor for three different values of cladding RI. **(D)** Resonance wavelength shift for different values of cladding refractive index in the improved sensor.

cladding RI of 1.33. When the refractive index of the cladding is increased, both MD and ED resonances shift towards longer wavelengths. The shift of both MD and ED resonances for different index values of the cladding are shown in Figure 1D. Sensitivity (S) is defined as the ratio of change in resonance wavelength ($\Delta\lambda$) to the change in refractive index (Δn). The sensitivity of this sensor is 192.50 nm/Refractive Index Unit (RIU) and 122.50 nm/RIU for MD and ED resonances, respectively. The figure of merit (FOM) is given by $S/FWHM$ and its values are 2.00 and 7.42 for MD and ED resonances, respectively. Though the sensitivities of the sensor are reasonably good, the values of FOM are very low due to the broad FWHM of both MD and ED resonances.

To increase the sensitivity as well as the FOM of the proposed sensor, the design of the unit cell is slightly modified. The schematic of the unit cell of the modified sensor is shown in Figure 2A. It has the following design parameters: Λ of 730 nm, W of 600 nm, and a 75 nm thick (along Y-direction) slot is etched at the center of the meta-atom. As discussed in (Barrios et al., 2007; Zhang et al., 2014; Meng et al., 2021; Yin, 2023), the presence of a slot between the meta-atoms, in the form of a meta-waveguide, will result in an enhancement of the electric field in the slot region. This enhancement of the electric field depends on the width, height, and shape of the slot. The enhanced electric field confinement in the slot adds to the interaction already present due to the meta-atom. When the cladding is a solution-based analyte, it is expected to fill the slot and cover the meta-atoms. The increase in contact area

between the cladding medium and the metasurface due to the presence of the slot leads to an increase in the interaction between the electromagnetic field and the cladding medium and aids in achieving better characteristics for sensing. The transmission spectrum of the improved sensor is computed for a Y-polarized normally incident plane-wave considering air as the cladding material. Figure 2B shows that now the MD and ED resonances are appearing at $\lambda \sim 1.21\ \mu m$ and $\lambda \sim 1.33\ \mu m$, respectively, for this improved design. In addition to that, the line-widths of both the resonances are very narrow as compared to the resonance line-widths in previous design as shown in Figure 1A. We have also investigated the dependency of transmission spectra on different structural parameters of the improved sensor and the results are shown in Supplementary Figure S2.

We have varied the periodicity (Λ), meta-atom width (W), meta-atom height (h), and channel width (gap) of the improved sensor and computed the transmission spectra for a cladding refractive index of 1.33. As shown in Supplementary Figure S2A, when the periodicity (Λ) increases, both the resonances shift towards the higher wavelength values. MD resonance shows more shift than the ED resonance. Thus, the gap between these two resonances reduces. In addition to that, line-widths of both the resonances increase with an increase in periodicity.

The effects of change in meta-atom width (W) are shown in Supplementary Figure S2B. As the width increases, both the resonances shift towards higher wavelengths as in the previous case. However, ED resonance shifts more than the MD

TABLE 1 Computed FWHM and Q-factors of the improved sensor for cladding RI values of 1.33, 1.41, and 1.49.

Cladding RI	FWHM$_{MD}$ (nm)	FWHM$_{ED}$ (nm)	Q$_{MD}$	Q$_{ED}$
1.33	5.2	12.9	252	109
1.41	4.1	13.5	326	106
1.49	3.7	14.7	368	99

resonance. The FWHM of both the resonances are also getting narrower as the width increases.

Supplementary Figure S2C is showing the effects of changing meta-atom height. The separation between the MD and ED resonances decreases with the increase in height. The FWHM of the resonance is also increasing with the increase in height. For a height of 240 nm, higher order resonance mode is also appearing at

the wavelength of 1.2 μm. With the increase in channel width (gap), the separation between two resonances decreases as shown in Supplementary Figure S2D.

For a good sensor, resonances which are distinctly apart and with lower resonance FWHM are preferred. To achieve high sensitivity and FOM, Λ = 730 nm, W = 600 nm, h = 220 nm, and a gap = 75 nm are chosen. All the other parameters and conditions are kept the same as mentioned in the previous case. To study RI sensing using this metasurface, the RI of the cladding is changed from 1.33 to 1.49 as before. Resulting transmission spectra of the sensor are shown in Figure 2C. For this sensor, MD and ED resonances are appearing at λ ~1.31 μm and λ ~1.41 μm, respectively, for a cladding RI = 1.33. The wavelength separation between MD and ED resonances is also reduced. When the RI of the cladding is increased, both MD and ED resonance wavelengths shift towards higher values. This wavelength shift for both MD and ED resonances for different RI values of the cladding is shown in
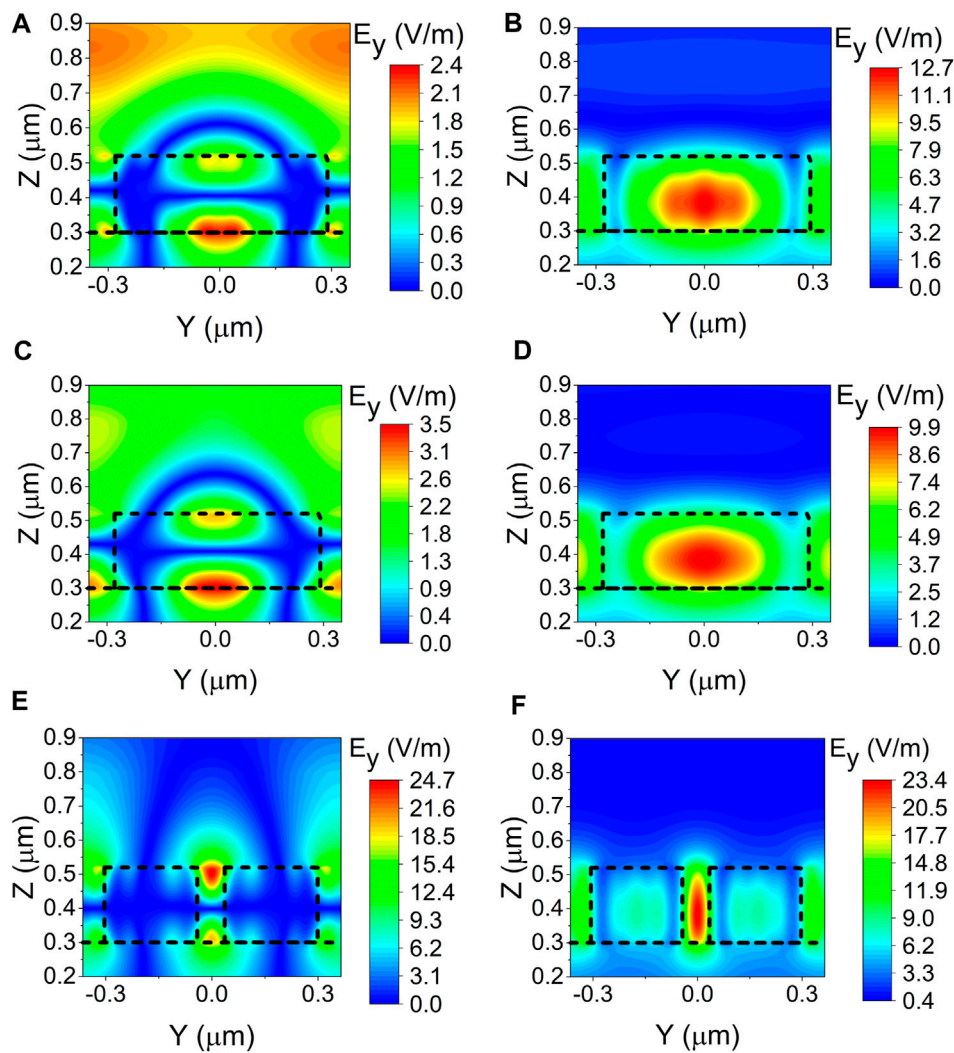
FIGURE 3
Amplitude distributions of the electric field ($|E_y|$) at the center of the unit cell in YZ-plane for **(A)** λ ~ 1.34 μm and **(B)** λ ~1.56 μm in metasurface with air cladding; **(C)** λ ~ 1.39 μm and **(D)** λ ~ 1.59 μm in proposed metasurface sensor with a cladding RI =1.33; and **(E)** λ ~ 1.31 μm and **(F)** λ ~1.41 μm in improved sensor with a cladding RI =1.33. The dashed black lines represent the boundary of the Si block. The color scale bar indicates the amplitude of the electric field.

TABLE 2 Comparison of the Existing RI sensors and Our Work.

References	Structure (method)	S_{max}(nm/RIU)	FOM_{max}
Liu et al. (2010)	Double cladding fibers (Experiment)	153.15	–
Hu et al. (2017)	Four holes in Si nanoblock unit (Simulation)	306.71	16.76
Ollanik et al. (2019)	Si nano-disks (Experiment)	323	5.4
This work	Si nano-pillars (Simulation)	325	62.50

Figure 2D with a uniform RI resolution of 0.04. The sensitivities of the sensor are 325.00 nm/RIU and 300.00 nm/RIU for MD and ED resonances, respectively. These are better than the values seen in Figure 1D. Corresponding improved FOM of the sensor are 62.50 and 23.26 for MD and ED resonances, respectively. So, the improved RI sensor has much higher sensitivity and FOM in comparison to the previous one. Computed FWHM and the quality (Q) factors of both MD and ED resonances are shown in Table 1 for three different RI values of the cladding. As the RI of the cladding increases, the FWHM of MD (ED) resonance is decreasing (increasing). As a result, Q-factor is also increasing (decreasing) for MD (ED) resonance.

3 Electric field profiles

We have also computed the electric and magnetic field distributions of light in two orthogonal planes at the center of the Si pillar for the two designs of metasurface discussed above, at their corresponding resonance wavelengths. For the first design with air cladding, the amplitudes of E_y for $\lambda \sim 1.34\ \mu m$ and $\lambda \sim 1.56\ \mu m$ are shown in Figures 3A, B, respectively. The amplitudes of E_y with a cladding index of 1.33 at $\lambda \sim 1.39\ \mu m$ and $\lambda \sim 1.59\ \mu m$ are shown in Figures 3C, D, respectively. Similarly, the amplitudes of E_y for $\lambda \sim 1.31\ \mu m$ and $\lambda \sim 1.41\ \mu m$ are shown in Figures 3E, F, respectively, for the improved sensor for a cladding RI =1.33. Corresponding amplitudes of H_x for all the configurations are shown exactly in the similar order in Supplementary Figure S3.

These spatial field distributions in Figure 3 and Supplementary Figure S3 indicate that the resonance at lower (higher) wavelength is of MD (ED) type (Iwanaga, 2018). The range of color scale bar indicates that the ED resonance is stronger than the MD resonance, as expected from its lower FWHM. In the case of improved sensor, it is seen that the field is highly confined in the central slot region which enhances the interaction between the electric-field of incident light and the surrounding medium. As a result, the field enhancement is higher than the earlier ones shown in Figures 3A–D.

Some existing dielectric RI sensor technologies are listed in Table 2 and the results of our work are shown in comparison. The improvement in the value of FOM in our design is clear.

4 Angle and polarization effects

We have computed the transmission spectra for both X (p-polarized) and Y-polarized (s-polarized) plane wave excitations of the metasurface shown in Figure 1A with air

cladding. At normal incidence, these two cases yield the same result as the unit cell is a square with sides along these axes. When the angle of incidence is increased, the two cases differ. We have computed the transmission spectra for different angles of incidence ranging from 0° to 20° with reference to the Z-axis considering both XZ and YZ as the planes of incidence.

Figures 4A, B are showing the computed transmission spectra for X and Y-polarized excitations, respectively, when XZ-plane is the plane of incidence. The dashed white lines in both the figures are used to represent the transmission minima due to MD and ED resonances at normal incidence. For p-polarized light, more than one dip appears in MD resonance when the angle of incidence is increased. Of the three minima seen, one is found to shift towards the ED resonance and crosses it at larger angles (not shown here). However, the wavelength of ED resonance remains unchanged as shown in Figure 4A. In the case of s-polarized light, both MD and ED resonances remain unchanged for the range of incidence angles considered in Figure 4B. The color scale bar indicates the magnitude of transmission. We have also seen that if the plane of incidence is changed to YZ-plane, the in-plane (p or Y) and out-of-plane (s or X) polarized light will produce the same results as shown in Figures 4A, B, respectively. The proposed metasurface is polarization sensitive for MD resonance at oblique angles of incidence.

However, in the improved design, the symmetry of the square shape of the meta-atom is broken by the introduction of the central slot. Due to the presence of the central slot, the design is not symmetric in the two orthogonal directions within the plane which are parallel to the sides of the meta-atom, unlike the first design. Therefore, the metasurface is polarization sensitive even for normal incidence. We have also seen that irrespective of the plane of incidence (i.e., YZ or XZ), normally incident Y-polarized plane-wave (when the electric field is oriented across the central slot) gives very sharp ED and MD resonances. But the same is not observed for X-polarized incident wave because the MD resonance is much broader than the ED resonance in it. At oblique incidence, more resonances of higher order are obtained and they are seen for both p-and s-polarizations. Therefore, this design gives the best performance for normal incidence (with a tolerance of ± 2°) for the light polarized along Y-axis.

5 Effects of temperature on resonances of the improved sensor

The effects of ambient temperature have also been investigated considering the improved sensor with a cladding index of 1.33. The thermo-optic coefficients of the Si and SiO_2 substrate are taken as
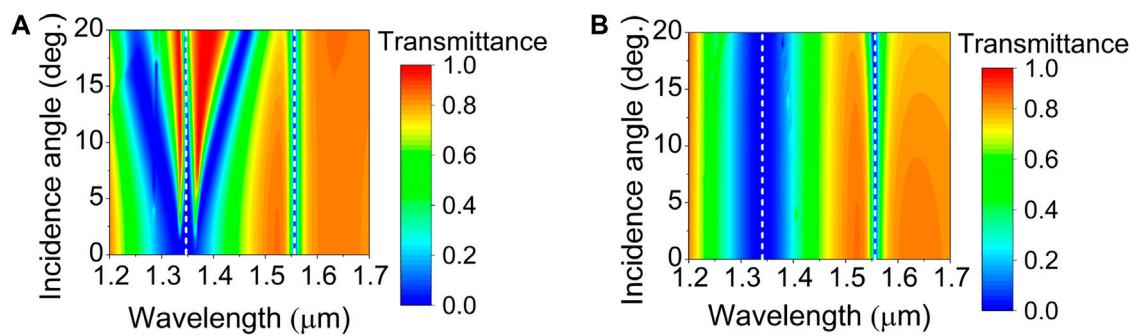
FIGURE 4
Transmission for different angles of incidence for **(A)** p-polarized (electric field is along *X*-axis) and **(B)** s-polarized (electric field is along *Y*-axis) plane wave excitations for the design shown in Figure 1A. The color scale bar indicates the value of transmittance.
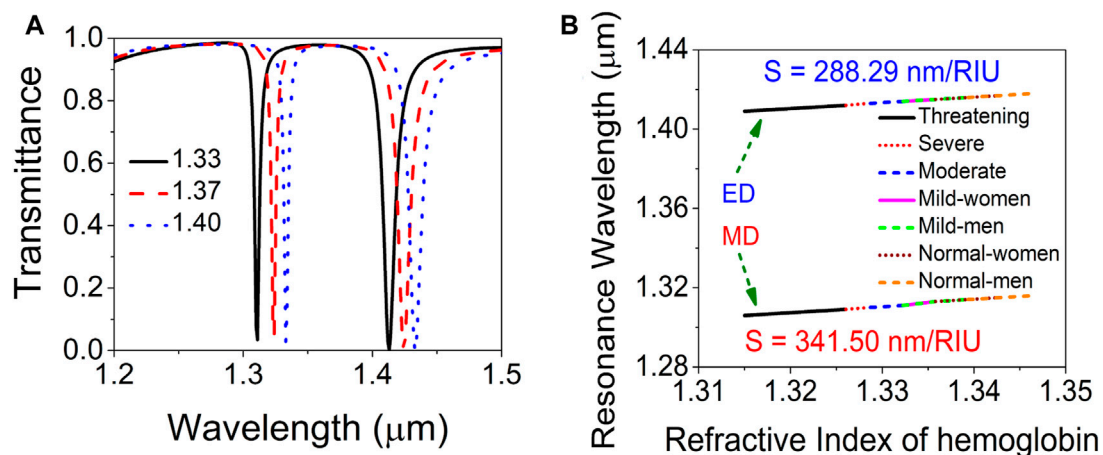

FIGURE 5
(A) Transmission spectra of the proposed sensor for application in anemia detection. **(B)** Resonance wavelength shift for different phases of anemia.

1.84×10^{-4} RIU/K (Okada and Tokumaru, 1984) and 8.6×10^{-6} RIU/K (Leviton and Frey, 2006), respectively. Computed resonance wavelength shifts for different temperatures in the range of $273–373K$ (correspond to $0–100°C$) are shown in Supplementary Figure S4. As the temperature increases, both the resonances shift to higher values linearly. However, the slopes of both the lines are very small of the order of $\sim 10^{-5}$ $\mu m/K$. This implies that the shift in resonance wavelengths due to an increase in ambient temperature of a couple of degrees may not be detected and therefore does not affect the performance of the improved sensor to any significant extent.

6 Improved all-dielectric sensor for anemia detection

Estimating the refractive index of bio-samples is crucial in the field of pathology. This can be used to diagnose diseases such as malaria, cancer, anemia, and tumor without a bodily intervention. The proposed sensor may not be suitable for all types of bio-samples

in its present form and may require some additional changes depending on the experimental needs. Here, we demonstrate the utility of the proposed improved all-dielectric sensor for anemia diagnosis in hematology test. Using a centrifuge, various components of the blood sample such as red blood cells (RBC), white blood cells (WBC), and platelets can be easily separated. Hemoglobin is the main component of the RBC in blood sample. The RI of RBC is given by Goldstone-Dale law (Lazareva and Tuchin, 2018a),

$$n_{RBC} = 0.75n_{water} + 0.25n_{hb} \qquad (1)$$

where, n_{water} and n_{hb} are RI of water and hemoglobin, respectively. The RI of RBC in normal scenario (healthy person) is 1.40. In the case of anemia, the concentration of hemoglobin decreases. As a result of that, RI of RBC also decreases. We have computed the transmission spectra of the sensor shown in Figure 2A for three different RI of the cladding as shown in Figure 5A. For non-anemic blood sample, the MD and ED resonances appear at ~ 1.33 μm and ~ 1.43 μm, respectively. When the RI of the blood sample reduces

below the normal value due to anemia, both the resonances show a blue-shift. Thus, from the value of resonance wavelengths, one can provide an initial diagnosis of whether the person is anemic or not.

In order to measure the severity of the anemia, we have considered nine different RI values ranging from 1.3150 to 1.3464 corresponding to the hemoglobin solutions with concentrations ranging from 0 g/L to 180 g/L in saline (Lazareva and Tuchin, 2018b). We have computed the resonance wavelengths for all these cladding RI values and the result is shown in Figure 5B. There are two lines corresponding to MD and ED resonance shifts as labeled in Figure 5B. In each line, different phases of anemia are shown in different segments. A change in RI of 0.01 implies a shift in resonance wavelength of 2.88 nm and 3.41 nm for the ED and MD resonances, respectively. These are detectable in standard spectrometers (Yang et al., 2019). So, by comparing with the position of resonance wavelength in Figure 5B, the severity of anemia can be inferred. The linear variation is a significant advantage.

The proposed all-dielectric metasurface sensors can be fabricated using standard complementary metal-oxide semiconductor (CMOS) fabrication facility. Optimized 220 nm thick Si layer can be deposited on SiO_2 substrate using plasma enhanced chemical vapour deposition (PECVD) method. Suitable electron sensitive resist is to be coated on the sample by spin-coating. After that, electron-beam lithography (EBL) can be directly used to transfer the patterns on the resist. The EBL alters the solubility of the resist in selective regions. Subsequently, the sample can be immersed in a suitable developer solution to remove the resist selectively. Once the resist is removed, the sample can be etched by reactive ion-etching (RIE) process to obtain the final metasurface sensor.

7 Conclusion

In this article, we have computationally investigated an all-dielectric metasurface as an RI sensor. The metasurface consists of a sub-wavelength array of Si meta-atoms present on SiO_2 platform. It has been seen that the metasurface shows both MD and ED resonances at two distinct wavelengths in the range of 1.2–1.7 μm. It has also been observed that both the resonances shift towards higher wavelengths as the RI of the surrounding cladding medium is increased from 1.33 to 1.49. We have shown that the performance of the sensor can be enhanced by increasing the interaction between EM-field and the surrounding medium with a modified structure of the meta-atoms. As a bio-medical application, we have proposed that the improved all-dielectric sensor can be used as an independent label-free optical platform to diagnose the presence of anemia, over the wide range of the mildest condition to the most threatening condition. This is due to the reported linear variation in refractive index for those conditions. In addition, the severity of anemia can be evaluated using the sensor in an entirely non-contact mode. The analysis provides a

significant wavelength shift of 2.88 nm and 3.41 nm for ED and MD resonances, respectively, for a refractive index change of 0.01, which is well within the accessible range of many hand-held spectrometers. This advantage is predominantly due to its loss-less performance arising from its dielectric nature for optical studies in the NIR wavelength range.

Data availability statement

The original contributions presented in the study are included in the article/Supplementary Material, further inquiries can be directed to the corresponding author.

Author contributions

DD–investigation, methodology, software, data analysis, writing-original draft. RV–supervision, funding acquisition, resources, writing-original draft. All authors contributed to the article and approved the submitted version.

Funding

Conflict of interest

The authors declare that the research was conducted in the absence of any commercial or financial relationships that could be construed as a potential conflict of interest.

Publisher's note

All claims expressed in this article are solely those of the authors and do not necessarily represent those of their affiliated organizations, or those of the publisher, the editors and the reviewers. Any product that may be evaluated in this article, or claim that may be made by its manufacturer, is not guaranteed or endorsed by the publisher.

Supplementary material

The Supplementary Material for this article can be found online at: https://www.frontiersin.org/articles/10.3389/fphot.2023.1234060/full#supplementary-material

References

Aieta, F., Genevet, P., Kats, M. A., Yu, N., Blanchard, R., Gaburro, Z., et al. (2012). Aberration-free ultrathin flat lenses and axicons at telecom wavelengths based on plasmonic metasurfaces. *Nano Lett.* 12, 4932–4936. doi:10.1021/nl302516v

Baranov, D. G., Zuev, D. A., Lepeshov, S. I., Kotov, O. V., Krasnok, A. E., Evlyukhin, A. B., et al. (2017). All-dielectric nanophotonics: The quest for better materials and fabrication techniques. *Optica* 4, 814–825. doi:10.1364/OPTICA.4.000814

Barrios, C. A., Gylfason, K. B., Sanchez, B., Griol, A., Sohlstrom, H., Holgado, M., et al. (2007). Slot-waveguide biochemical sensor. *Opt. Lett.* 32, 3080–3082. doi:10.1364/OL.32.003080

Chen, W., Li, M., Zhang, W., and Chen, Y. (2023). Dual-resonance sensing for environmental refractive index based on quasi-bic states in all-dielectric metasurface. *Nanophotonics* 12, 1147–1157. doi:10.1515/nanoph-2022-0776

DiffractMod (RSoft) (2004). *DiffractMod (RSoft)*.

Gao, X., Han, X., Cao, W.-P., Li, H. O., Ma, H. F., and Cui, T. J. (2015). Ultrawideband and high-efficiency linear polarization converter based on double v-shaped metasurface. *IEEE Trans. Antennas Propag.* 63, 3522–3530. doi:10.1109/TAP.2015.2434392

Horie, Y., Arbabi, A., Arbabi, E., Kamali, S. M., and Faraon, A. (2018). High-speed, phase-dominant spatial light modulation with silicon-based active resonant antennas. *ACS Photonics* 5, 1711–1717. doi:10.1021/acsphotonics.7b01073

Howes, A., Zhu, Z., Curie, D., Avila, J. R., Wheeler, V. D., Haglund, R. F., et al. (2020). Optical limiting based on huygens' metasurfaces. *Nano Lett.* 20, 4638–4644. doi:10.1021/acs.nanolett.0c01574

Hu, J., Lang, T., and hua Shi, G. (2017). Simultaneous measurement of refractive index and temperature based on all-dielectric metasurface. *Opt. Express* 25, 15241–15251. doi:10.1364/OE.25.015241

Iwanaga, M. (2018). All-dielectric metasurfaces with high-fluorescence-enhancing capability. *Appl. Sci.* 8, 1328. doi:10.3390/app8081328

Khorasaninejad, M., and Capasso, F. (2017). Metalenses: Versatile multifunctional photonic components. *Science* 358, eaam8100. doi:10.1126/science.aam8100

Lazareva, E. N., and Tuchin, V. V. (2018a). Blood refractive index modelling in the visible and near infrared spectral regions. *J. Biomed. Photonics & Eng.* 4, 010503. doi:10.18287/JBPE18.04.010503

Lazareva, E. N., and Tuchin, V. V. (2018b). Measurement of refractive index of hemoglobin in the visible/nir spectral range. *J. Biomed. Opt.* 23, 1. doi:10.1117/1.JBO.23.3.035004

Lee, Y., Kim, S.-J., Park, H., and Lee, B. (2017). Metamaterials and metasurfaces for sensor applications. *Sensors* 17, 1726. doi:10.3390/s17081726

Leviton, D. B., and Frey, B. J. (2006). "Temperature-dependent absolute refractive index measurements of synthetic fused silica," in *Proc. Of SPIE*. Editors E. Atad-Ettedgui, J. Antebi, and D. Lemke, 6273, 62732K.

Liu, H., Pang, F., Guo, H., Cao, W., Liu, Y., Chen, N., et al. (2010). In-series double cladding fibers for simultaneous refractive index and temperature measurement. *Opt. Express* 18, 13072–13082. doi:10.1364/OE.18.013072

Meng, Y., Chen, Y., Lu, L., Ding, Y., Cusano, A., Fan, J. A., et al. (2021). Optical meta-waveguides for integrated photonics and beyond. *Light Sci. Appl.* 10, 235. doi:10.1038/s41377-021-00655-x

Ni, X., Emani, N. K., Kildishev, A. V., Boltasseva, A., and Shalaev, V. M. (2012). Broadband light bending with plasmonic nanoantennas. *Science* 335, 427. doi:10.1126/science.1214686

Okada, Y., and Tokumaru, Y. (1984). Precise determination of lattice parameter and thermal expansion coefficient of silicon between 300 and 1500 k. *J. Appl. Phys.* 56, 314–320. doi:10.1063/1.333965

Ollanik, A. J., Oguntoye, I. O., Hartfield, G. Z., and Escarra, M. D. (2019). Highly sensitive, affordable, and adaptable refractive index sensing with silicon-based dielectric metasurfaces. *Adv. Mater. Technol.* 4, 1800567. doi:10.1002/admt.201800567

Ozbay, E. (2006). Plasmonics: Merging photonics and electronics at nanoscale dimensions. *Science* 311, 189–193. doi:10.1126/science.1114849

Shao, J., Li, J., Wang, Y.-H., Li, J.-Q., Chen, Q., and Dong, Z.-G. (2014). Polarization conversions of linearly and circularly polarized lights through a plasmon-induced transparent metasurface. *J. Appl. Phys.* 115, 243503. doi:10.1063/1.4885769

Tittl, A., Leitis, A., Liu, M., Yesilkoy, F., Choi, D.-Y., Neshev, D. N., et al. (2018). Imaging-based molecular barcoding with pixelated dielectric metasurfaces. *Science* 360, 1105–1109. doi:10.1126/science.aas9768

Tong, L., Wei, H., Zhang, S., and Xu, H. (2014). Recent advances in plasmonic sensors. *Recent Adv. plasmonic sensors* 14, 7959–7973. doi:10.3390/s140507959

West, P. R., Stewart, J. L., Kildishev, A. V., Shalaev, V. M., Shkunov, V. V., Strohkendl, F., et al. (2014). All-dielectric subwavelength metasurface focusing lens. *Opt. Express* 22, 26212–26221. doi:10.1364/OE.22.026212

Yang, Z., Xia, L., Li, S., Qi, R., Chen, X., and Li, W. (2019). Highly sensitive refractive index detection based on compact hsc-spr structure in a microfluidic chip. *Sensors Actuators A Phys.* 297, 111558. doi:10.1016/j.sna.2019.111558

Yin, X. (2023). Effective optical biosensing using a graphene-based metasurface of asymmetric split silicon bars. *Optik* 287, 171047. doi:10.1016/j.ijleo.2023.171047

Yu, N., Genevet, P., Kats, M. A., Aieta, F., Tetienne, J.-P., Capasso, F., et al. (2011). Light propagation with phase discontinuities: Generalized laws of reflection and refraction. *Science* 334, 333–337. doi:10.1126/science.1210713

Zhang, C., Xue, T., Zhang, J., Liu, L., Xie, J., Wang, G., et al. (2022). Terahertz toroidal metasurface biosensor for sensitive distinction of lung cancer cells. *Nanophotonics* 11, 101–109. doi:10.1515/nanoph-2021-0520

Zhang, J., Liu, W., Zhu, Z., Yuan, X., and Qin, S. (2014). Strong field enhancement and light-matter interactions with all-dielectric metamaterials based on split bar resonators. *Opt. Express* 22, 30889–30898. doi:10.1364/OE.22.030889